



Imag(in)ing the continental lithosphere

Alan Levander*, Fenglin Niu, Cin-Ty A. Lee, Xin Cheng

Department of Earth Science, Rice University, Houston, Texas 77005, USA

Accepted 28 November 2005

Available online 28 February 2006

Abstract

This paper is primarily concerned with seismically imaging details in the mantle at an intermediate scale length between the large scales of regional and global tomography and the small scales of reflection profiles and outcrops. This range is roughly $0.1-1 \text{ km} < a < 10-10^2 \text{ km}$, where a is the scale. We consider the implications of several models for mantle evolution in a convecting mantle, and possible scales present in the non-convecting tectosphere. Reflection seismic evidence shows that the structures preserved from continental accretion within and at the margins of the Archean cratons are subduction related, and we use subduction as an analog for scales left by past events. In modern orogenic belts we expect to find subduction structures, small scale upper mantle convection structures, and basalt extraction structures. We examine some of the scales that are likely formed by orogenic processes.

We also examine the seismic velocity and density contrasts expected between various upper mantle constituents, including fertile upper mantle, depleted upper mantle, normal and eclogitized oceanic crust, and fertile mantle with and without partial melt. This leads directly to predicting the size of seismic signals that can be produced by specular conversion, and scattering from layers and objects with these contrasts.

We introduce an imaging scheme that makes use of scattered waves in teleseismic receiver functions to make a depth migrated image of a pseudo-scattering coefficient. Image resolution is theoretically at least an order of magnitude better than travelt ime tomography. We apply the imaging scheme to three data sets from 1) the Kaapvaal craton, 2) the Cheyenne Belt, a Paleoproterozoic suture between a protocontinent and an island arc, and 3) the Jemez Lineament, a series of aligned modern volcanic structures at the site of a Proterozoic suture zone. The Kaapvaal image, although not defining a unique base of the tectosphere, shows complicated “layered” events in the region defined as the base of the tectosphere in tomography images. The image of the transition zone discontinuities beneath the Kaapvaal craton is remarkable for clarity. The migrated receiver function image of the upper mantle beneath the Cheyenne belt is complicated, more so than the tomography image, and may indicate limitations in the receiver function imaging system. In contrast the Jemez Lineament image shows large-amplitude negative-polarity layered events beneath the Moho to depths of $\sim 120 \text{ km}$, that we interpret as melt-containing sills in the upper mantle. These sills presumably feed the Quaternary–Neogene regional basaltic volcanic field.

© 2006 Elsevier B.V. All rights reserved.

Keywords: Continental lithosphere; Receiver functions; Kirchhoff depth migration; Kaapvaal Craton; Jemez Lineament

1. Introduction

The development of portable, observatory quality broadband seismographs in large numbers has both changed our understanding of the heterogeneity of the

* Corresponding author.

E-mail address: alan@rice.edu (A. Levander).

mantle (for example, Humphreys and Dueker, 1994a, b), and allowed us to consider new means of imaging with earthquake waves (see for example, Levander and Nolet, 2005, and papers therein). This paper discusses aspects of both likely mantle heterogeneities and high resolution imaging methods that use wavefield depropagation and focusing of earthquake recordings to observe details of mantle heterogeneity. The approach of this paper is very similar to the approach we would take to design an experiment: We estimate the scales of heterogeneities that we expect to find in the upper mantle beneath the continents. Since the structure of the mantle at small to intermediate scales (1–30 km) is poorly known, we refer to developmental models for the mantle and the continents as well as available field data. We estimate the petrophysical contrasts that are likely at these heterogeneities using a variety of techniques, including the results of stoichiometric seismic velocity calculations. Then we determine the array requirements to observe these features, and briefly discuss the imaging method we use to achieve this resolution, a pre-stack Kirchhoff depth migration of receiver functions designed to image with P to S converted waves from teleseisms.

We conclude showing depth migrated images from the Kaapvaal craton in southern Africa that extend below the transition zone, and images of the upper mantle to ~200 km depth from the western North American orogenic plateau.

2. Elements of the continental lithosphere

The standard model of the continental lithosphere is largely due to Jordan (1978, 1988, see also Pollack, 1986; among others), in which a highly depleted relatively low density upper mantle layer, known as the tectosphere, extends to great depths beneath the continents. Jordan proposed the isopycnic hypothesis, which states that the negative thermal buoyancy of cold cratonic mantle is exactly compensated at every depth by an intrinsic chemical buoyancy. The intrinsic chemical buoyancy of cratonic mantle is a consequence of its highly melt-depleted character, manifested by high Mg#s (90–93; $Mg\# = Mg / (Mg + Fe) \times 100$) and low densities compared to the fertile convecting mantle (Mg# 88–89). The highly melt-depleted character of cratonic mantle is thought by some to be the result of higher ambient mantle temperatures that led to larger degrees of melt extraction in the Archean and Proterozoic.

Although the details of formation of the tectosphere are debated, various authors have invoked a combina-

tion of primary differentiation combined with subduction-like processes that further depleted the mantle wedge material and caused secondary differentiation of the crust followed by proto-continent collision to build the continental masses. Jordan described this process as lateral advection of mass. Deep reflection profiles that image subduction like structures to depths as great as 120 km in Proterozoic rather than Archean terranes (Cook et al., 1998) have led to the suggestion that the cratonic mantle was formed by lateral stacking of successive subducting plates forming the cratons from inside out by underside accretion of partially depleted Precambrian oceanic plates. In this case a relaxed isopycnic hypothesis is required, as the stack of plates would produce a mass column that on average is balanced against the mass of the mantle column under the oceans, but wouldn't produce equivalent densities at every depth.

The depth to which the tectospheric mantle extends is still a hotly debated topic (e.g., Polet and Anderson, 1995), although most tomographic images of the craton show high velocity roots extending to at least 200 km depth, and in some cases to depths greater than 300 km (e.g., Grand, 1994; Van der Lee and Nolet, 1997). Since body wave tomographic images smear anomalies along ray paths and the angular bandwidth is limited to a small set of fairly steep angles, the depth to which high velocities extend under the craton, and the transition from tectosphere to asthenospheric mantle is usually obscured. Unfortunately the sources used in conventional active source seismology are generally too weak to probe the deeper parts of the cratonic mantle, making the base of the tectosphere an exploration target in teleseismic and regional seismology.

As the mantle is divided between a dynamic, evolving oceanic system and a stable continental system, and seismic investigations are limited in a variety of ways, we refer to mantle scaling and convection models to provide predictions of scales that we might find in areas where the continental mantle has been remobilized, as under the orogenic belts, and the scales that are residues from continental accretion in the stable Precambrian mantle. We consider a few representative end members of the many models for mantle circulation, and relate them to observations of mantle scales made from seismic reflection data and outcrops.

2.1. Models of the mantle: structures from subduction processes

It has been long recognized that the cratonic crust is formed of paraautochthonous island arc and marginal

basin lithologies, appearing as the “granite-greenstone” belts in the Canadian Shield and the Australian cratons. Lithoprobe reflection and refraction data document these subduction related structural elements of the Archean crust extremely well (Calvert et al., 1995). Tomography images of the cratonic mantle provide the largest scales of lateral heterogeneity, generally on the order of 10s to 100s of kilometers (e.g., James et al., 2001; Grand, 1994), but as noted above, unfortunately provide relatively poor vertical resolution. For greater detail in the uppermost mantle we have to turn to the relatively limited number of seismic reflection profiles showing unambiguous upper mantle reflections. The Abitibi–Opatica profile of Calvert et al. (1995) shows upper mantle reflections in the Superior province, in central Canada, documenting recognizable subduction structures to depths of 70 km in the craton that are interpreted to date back to at least 2.69 Ma. Another Lithoprobe reflection profile, SNORCLE, which crosses the Proterozoic Wopmay orogen and the western edge of the Archean Slave Province, shows a remarkable series of upper mantle reflections that extend to ~100 km depth (Bostock, 1998; Cook et al., 1998), giving the appearance of an accreted mantle lithosphere created by progressive stacking of Precambrian plates from below and from the inside of the craton out (Cook et al., 1998; Snyder, 2002; Cooper et al., submitted for publication). Although these mantle structures are Proterozoic rather than Archean, they can be interpreted as conforming to the standard cratonic developmental model with the geometry providing an intuitive understanding of lateral advection and accretion. The buoyant Precambrian plates sheath the continental cores in successive accreted layers, with the plates deforming the peripheries of the cratonic cores as they accrete.

The SNORCLE profile is also important because receiver function images made with teleseismic data from the Yellowknife array at the eastern edge of the profile show S-wave conversion events coinciding with a number of prominent mantle reflections (Bostock, 1998; Fig. 1). This observation confirms that fine scale, $O(<1 \text{ km})$, features seen in high frequency (10–50 Hz) reflection data also produce recognizable signals in the lower frequency teleseismic data (0.03–0.2 Hz), providing two different seismic probes that are capable of detecting fine scale mantle structures across ~3 orders of combined bandwidth. We expand on imaging considerations further in a later section, but note here that reflection profiles and converted wave images sense overlapping scales, and that converted wave images are not depth limited in penetration like reflection profiling.

Outcrop information on mantle scales is generally limited to the small number of exposures of usually fragmented ophiolites and peridotite massifs. Outcrop scale (1–100 cm) features seen in the Beni–Bousera peridotite massif led Allegre and Turcotte (1986) to propose the “marble-cake” mantle model and Kellogg and Turcotte (1990) to develop a predictive model for the scale range to be expected. The marble-cake represents one end member of a large class of mantle circulation models. The marble-cake model envisions that subducted oceanic crust is eclogitized (i.e., converted to a garnet bearing pyroxenite) during subduction, and then is continuously folded, refolded and thinned until the standard oceanic crustal thickness (~6 km) is reduced to garnet pyroxenite layers that are centimeters thick. Although this is an extreme model of convective thinning, the marble-cake mantle nonetheless provides a useful end member for seismic imaging considerations in that it predicts a continuous range of scales as a function of time since subduction, with the eclogitized oceanic crust thinning by a factor of 10^5 , and the thicknesses obeying a simple power law behavior. Although folding and thinning is not a mixing process per se, heterogeneity resulting from folding and thinning the oceanic crust is dispersed fairly uniformly throughout the mantle, regardless of the viscosity structure of the mantle adopted (e.g., Hunt and Kellogg, 2001).

Fig. 2 is the frequency distribution of layer thicknesses from the Beni–Bousera plotted with those derived from the SNORCLE profile. The former are the raw data on which the marble-cake model was developed. The combined set of observations shows a remarkable power law behavior over 5 orders of magnitude. If we accept the marble-cake mantle model, the scale change is equivalent to time since subduction, with the largest scales representing the point at which oceanic crust is subducted (i.e., it is 6–10 km thick), and the smaller scales representing the point at which chemical diffusion begins to dominate over further thinning ($O(10^{-2} \text{ m})$). If one does not accept the marble-cake mantle model, Fig. 2 can be interpreted as simply a self-affine (fractal) distribution of scales expected in the upper mantle. For seismic imaging purposes the interpretation of why the power law exists is of secondary concern to the fact that it does exist.

Other models that describe likely upper mantle heterogeneity include upper mantle reservoir models (Kellogg et al., 2002), which make some effort to estimate the scales of depleted mantle, but with a focus on geochemical sampling rather than seismic sampling, and the more physically qualitative SUMA model

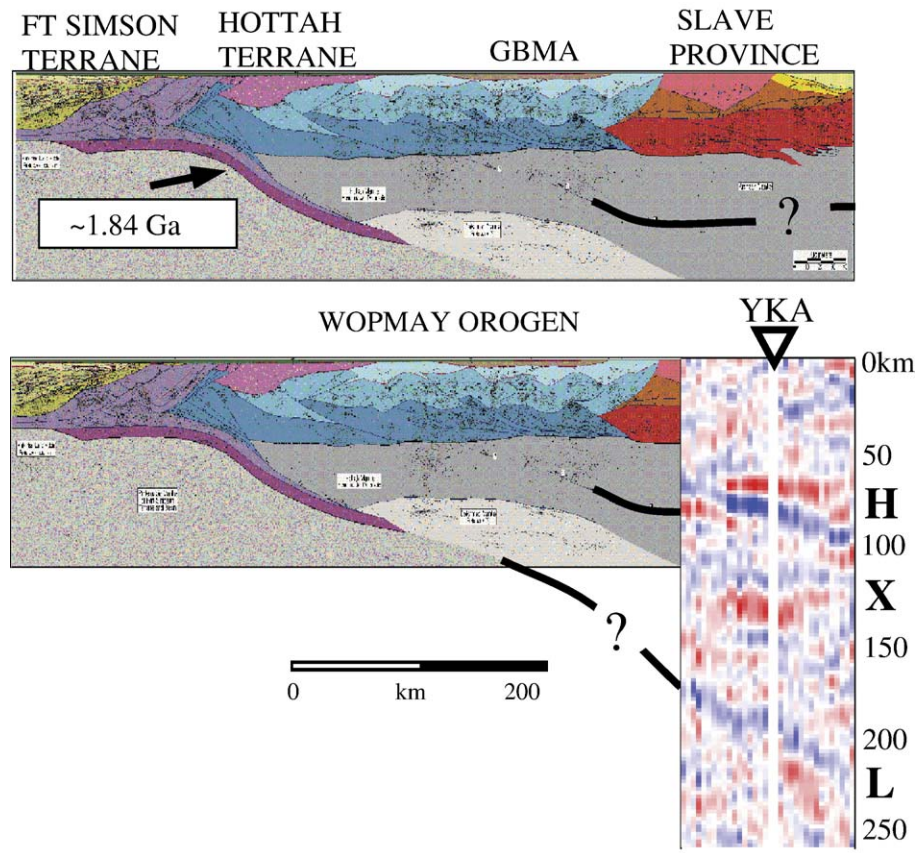


Fig. 1. Top: The SNORCLE profile from the Proterozoic Wopmay orogen and the edge of the Slave Craton (from Bostock, 1998). The reflection section shows subduction features that can be traced from the crust into the upper mantle to depths of about 120 km. In particular, the mantle looks as though it consists of accreted lithospheric slabs. Note also that the crust is a thrust belt with stacking of layers from the top down to the Moho. In analogy, the mantle is composed of layers that have been underthrust from the Moho down. Bottom: The SNORCLE profile with SH component receiver functions from earthquakes at a range of distances. The much lower frequency receiver functions see converted wave events from the layering observed in the mantle in the higher frequency reflection data. This section illustrates that mantle features are observable over a broad bandwidth, and can be imaged with multi-band data. Bostock interprets the SH receiver function events as being generated by anisotropic structures.

(Meibom and Anderson, 2003) put forward as an explanation for the various geochemical anomalies that have led to the prediction of mantle reservoirs of different composition (Fig. 3). Kellogg et al. (2002) conclude that the marble-cake is compatible with their reservoir model, as are the several primary geochemical observations. They also predict that any heterogeneity will be mixed in such a way as to produce a self-affine range of scales with time (Fig. 3). The primary difference between the Kellogg et al. (2002) reservoir model and SUMA (Statistical Upper Mantle Assemblage and/or Sampling Upon Melting and Averaging), is that heterogeneity in the latter is attributed to the inability of oceanic lithosphere less than 20 Myr old to subduct to appreciable depths. Subducting slabs less than 20 Myr old are thermally positively buoyant relative to asthenospheric mantle. Whereas older slabs

will descend to join the overall mantle circulation system, slabs under 20 Myr old will fragment into pieces whose sizes are determined by the fragmentation scales of the plate during subduction, and will remain dispersed in the upper mantle. We infer that the resulting structure of the upper mantle will be largely random in nature as the Earth evolves. Both the reservoir model and SUMA predict that zones of the upper mantle that are producing melt will average the chemistry of the background mantle with the fragments that are caught up in the thermal process producing the melt. Meibom and Anderson (2003) attribute variations in melt geochemistry to local averaging during melting and thereby attempt to explain the different chemistries of mantle melts without recourse to hidden reservoirs.

These models are useful in that they predict a continuous range of (self-affine) structures, and a

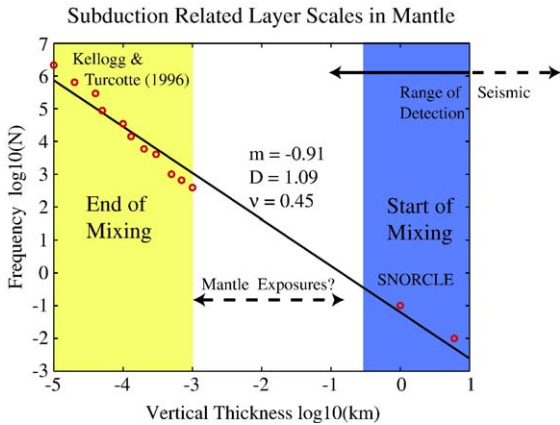


Fig. 2. Histogram of log frequency of occurrence versus log thickness for layering in the Beni-Bousera ophiolite (from Kellogg and Turcotte, 1990), with similar measurements made by us on the SNORCLE profile (see Fig. 1). Allegre and Turcotte (1986) and Kellogg and Turcotte (1990) interpret the layering as thinned eclogitized oceanic crust intermixed with peridotite. In SNORCLE the thicknesses are associated with layering associated with subducted oceanic crust. The observations show a remarkable linear relationship of log(frequency) vs. log(thickness) over 6 orders of magnitude. If one accepts the marble-cake mantle hypothesis (Allegre and Turcotte, 1986; see text), then the large scales (1–10 km) are the initial condition (subduction of the oceanic crust), and the smallest scales (10–5 km) are the final condition (where chemical diffusion begins to dominate over thinning and folding). If one doesn't accept the marble-cake mantle hypothesis, then the diagram indicates a simple relationship between occurrence and thicknesses of oceanic crust/garnet pyroxenite layering embedded in mantle peridotites.

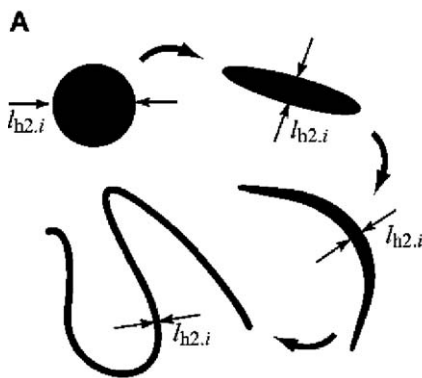
randomization of the upper mantle through imperfect subduction that produces a distribution of scales that is probably also self-affine. The models have oceanic

crustal thickness as one outer scale of heterogeneity, but the marble-cake predicts this scale is mechanically refined, whereas SUMA does not explicitly comment on it. If the fragments of oceanic lithosphere are caught up in upper mantle circulation they are presumably subject to the same folding and thinning processes leading to time dependent fractal scaling, or are perhaps preserved and merely rotated.

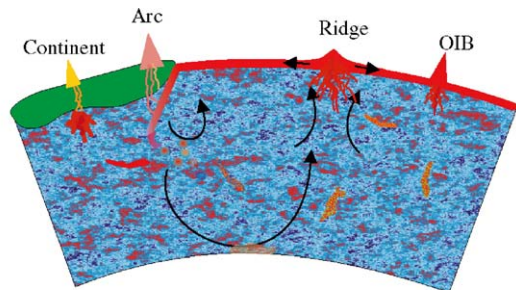
The marble-cake predicts an almost infinite scale in the trench parallel direction, whereas SUMA would have that scale regulated by the fragmentation length of the plate. The minimum scale in SUMA would result from the smallest fragmentation distance. In the marble-cake, the outer scale in the subduction normal direction could be on the order of the mean distance between transform faults. In SUMA the subduction normal scale and subduction parallel scales would likely be smaller, and would correspond to the fault distances observed in highly deformed young plates such as the Gorda (Gulick et al., 2001) where fragmentation occurs over 10s of kilometers.

2.2. Seismic detection

Seismic detection is a function of both mechanical contrast and object size, and requires that the mechanical contrasts between an object and its surroundings are large enough to produce a detectable signal. Detectable in this case means a signal is large in amplitude in comparison to the level of background and signal generated noise. Objects smaller than a Fresnel zone in size all produce diffracted waves of similar spatial



Stretching and folding a heterogeneity: From Kellogg et al., 2002.



SUMA: From Meibom and Anderson, 2003

Fig. 3. Left: Folding and stretching a heterogeneity. From Kellogg et al., 2002. Right: Schematic cross-section of upper mantle (to ~1000 km depth) in SUMA model (Meibom and Anderson, 2003). We infer that the young plates will fragment according to the fault systems developed during the plates' residence at the surface. Young subducted plate fragments may be folded and stretched as in A.

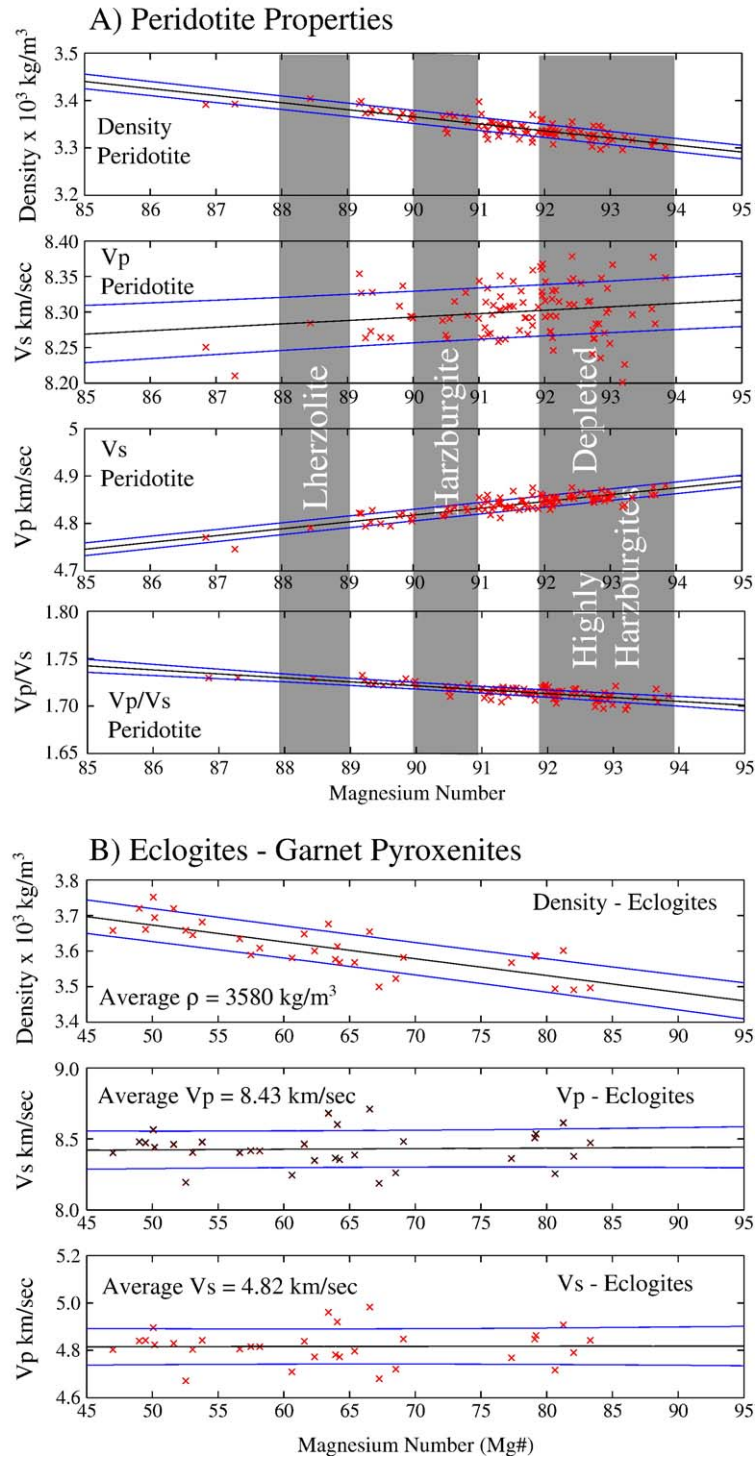


Fig. 4. A) Peridotite density, compressional and shear velocities, and V_p/V_s ratios as a function of magnesium number at standard temperature and pressure (modified after Lee, 2003). Both V_p and V_s increase with Mg#, i.e., with depletion, whereas density and V_p/V_s ratio decrease with Mg#. The density and V_s variations between lherzolite and a depleted peridotite are $\sim 2\%$ in magnitude. B) Density, compressional and shear velocities in eclogites (garnet pyroxenites) as a function of Mg# at standard temperature and pressure (after Cheng et al., unpublished). The V_p , V_s , and V_p/V_s ratio (average $V_p/V_s = 1.75$) are almost constant as a function of Mg#, whereas density decreases more than 5% across the range of observed eclogites.

extent. In the previous sections we have discussed the scales of structures expected in the mantle. We can estimate the petrophysical contrasts in the mantle that are introduced by subduction or by basalt extraction. We start with the simplified extraction of basalt from fertile lherzolite at the mid-ocean ridge:

lherzolite → harzburgite + basalt

Assigning fertile lherzolite (Mg# ≈ 88.5) as the reference density and velocities, we can write

$$\delta\rho/\rho = 0(\text{lherzolite}) \rightarrow (-1\% \text{ to } -2\%, \text{ harzburgite}) + (-10\%, \text{ basalt})$$

$$\delta V_p/V_p = 0 \rightarrow (+0.5\% \text{ to } +1.0\%) + (-14\% \text{ to } -16\%)$$

$$\delta V_s/V_s = 0 \rightarrow (+1\% \text{ to } +1.5\%) + (-16\% \text{ to } -23\%)$$

where the absolute values are summarized in Fig. 4A from stoichiometric calculations (Lee, 2003), and values for the oceanic crust were taken from Christensen and Salisbury (1975), and Christensen (1978). Upon subduction to depths of 40–60 km and greater the petrophysical properties of basaltic composition crust are altered due to eclogitization, whereas the harzburgite remains unchanged (Fig. 4B, Cheng et al., unpublished):

harzburgite + basalt → harzburgite + eclogite.

Still using lherzolite as the reference mantle

$$\Delta\rho/\rho = (-1\% \text{ to } -2\%, \text{ harzburgite}) + 5.5\% (\text{eclogite})$$

$$\delta V_p/V_p = (+0.5\% \text{ to } +1.0\%) \text{ to } (+2\%)$$

$$\delta V_s/V_s = (+1\% \text{ to } +1.5\%) + (+0.5\%).$$

These relations are summarized in Fig. 5. We can predict the strength of the P to S scattering from an object and the P to S conversion at an interface using these values in the scattering coefficients of Wu and Aki (1985) and the P to S reflection/transmission coefficients for continuous interfaces (Aki and Richards, 1980). The P to S forward scattering response for an eclogite imbedded in a fertile mantle (lherzolite) is shown in Fig. 6a, with comparisons to P to S scattering from the contrast at the Moho, and the 660 discontinuity. The transmission coefficients for the same planar interfaces are shown in Fig. 6b. The P to S scattering response of an embedded eclogite body is about one third that produced by the Moho, and is due almost entirely to the increase in density resulting from eclogitization.

The end member models of mantle circulation predict minimum scales at the initiation of subduction of at least

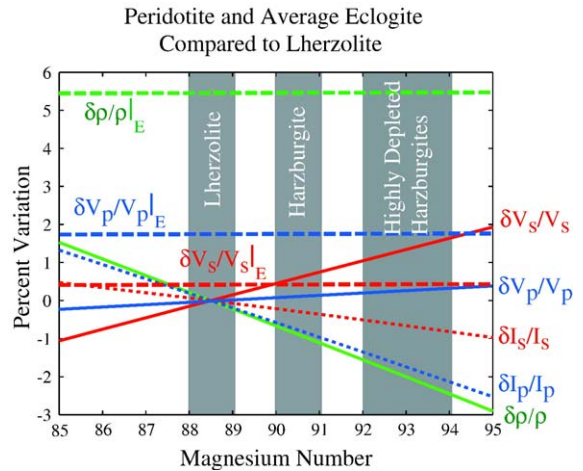


Fig. 5. A: Density, velocity, and impedance fluctuations of average eclogite, and peridotite compared to an average lherzolite (Mg# 88.5). Comparisons to eclogite are subscripted E, unsubscripted perturbations are compared to peridotite, and cross the abscissa at Mg# 88.5.

6 km by 10's to 100's of kilometers. Some of these scales appear to persist in the mantle. Large tabular bodies will behave as specular converters to short seismic wavelengths, smaller more equidimensional bodies resulting from slab fragmentations will act like point scatterers. In either case, P to S conversions from such bodies will produce detectable signals at dense seismic arrays, provided they arrive in a time window devoid of other significant arrivals.

Seismic observations at a number of arrays have been used to estimate scales of heterogeneity from seismic waves that scatter near the core–mantle boundary (e.g., Cleary and Haddon, 1972), in the whole mantle (Hedlin and Shearer, 2000), and in the mid-mantle beneath the southern Pacific (Kaneshima and Helffrich, 1998, 1999; Niu et al., 2003). Niu et al. (2003) observed a tabular body, ~12 by 100 by 100 km, at 1115 km depth beneath the Mariana subduction zone at 24.25°N 144.75°E. The body, which they interpret as an oceanic crustal layer, has S velocity reduced by 2–6% and density increased by 2–9% relative to the surrounding mantle.

2.3. Models of the mantle: structures from basalt extraction processes

Sources of information on the structures to be expected from zones of basalt extraction include natural source seismic images made over spreading ridges, and exposures of the upper mantle available from ophiolites. Unfortunately, active source seismic methods cannot generally penetrate far below crustal depths at the

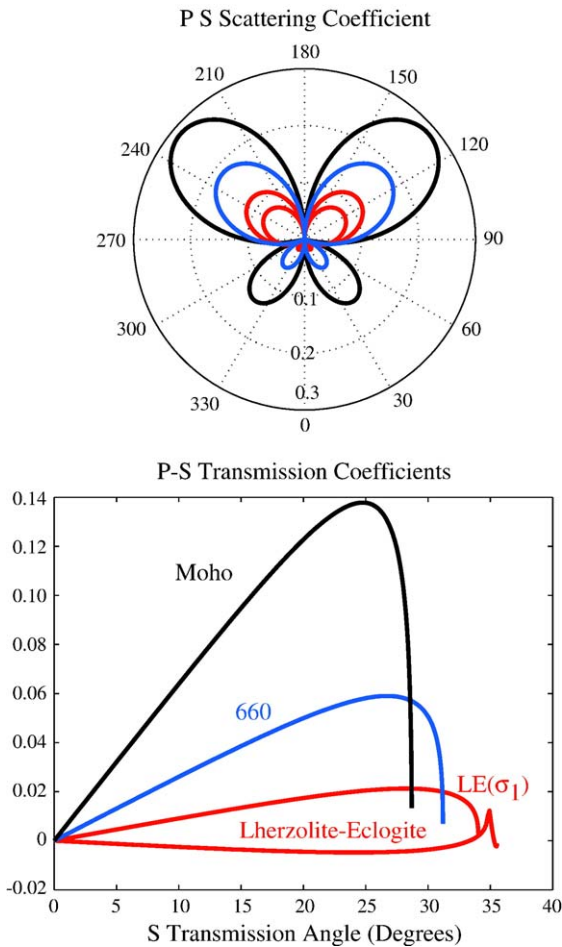


Fig. 6. P to S scattering coefficients (top) and P to S conversion coefficients (bottom) as a function of scattering angle for the perturbation at an average continental Moho (Christensen and Mooney, 1995), the PREM 660 discontinuity (Dziewonski and Anderson, 1981), an average lherzolite–average eclogite contrast, and a 1σ increase in lherzolite properties compared to average eclogite (which changes the sign of the velocity perturbation). P to S converted/scattered waves from eclogitized oceanic crust against a lherzolite mantle should be $\sim 0.1/0.3$ the size of events from the Moho, and $0.15/0.5$ the amplitude of events from the 660. These signal levels should be detectable in the upper mantle except where crustal multiples dominate the image.

spreading ridges due to high attenuation in the upper mantle.

The results of the MELT Experiment (MELT Seismic Team, 1998) provide outer scales on the basalt extraction region beneath a fast spreading ridge, the East Pacific Rise. A combination of teleseismic body and surface wave studies show that the region with reduced seismic velocities has a triangular cross-section with the apex under the axial ridge, extends over 650 km laterally, and shows a pronounced asymmetry toward the west. The region is 150–175 km deep. The zone of primary melting and lowest velocities is smaller, being

roughly 400 km across, and extending to ~ 100 km depth immediately below the ridge. No structural details within this zone are available from seismic data. Surface wave inversions (Webb and Forsythe, 1998) show shear wave reductions of 12.5% with respect to normal lid S velocities at 75 km depth beneath the ridge crest, with velocities at this depth increasing gradually away from the ridge, but how the velocity heterogeneity is distributed is unclear.

Evidence of the fine structure immediately below the oceanic Moho is provided by ophiolite exposures. Dunite bodies of variable thickness and length embedded in a harzburgite matrix are believed to be conduits for melt to reach the relatively small magma chamber beneath the spreading center. From the Oman ophiolite Braun and Keleman (2002) have measured a self-affine distribution of thicknesses of the dunite across 4 orders of magnitude (1 cm to 100s m), and have estimated that the largest likely dunite body is ~ 3 km in thickness, although none of this size was observed in the limited exposure available. Although Braun and Keleman (2002) didn't attempt to measure the length of the bodies their photographic evidence suggests an aspect ratio of at least 3:1.

The dunites without melt are not substantially different from the harzburgite matrix in velocity or density, however, addition of 1% basaltic melt to the channels changes the material properties substantially. We can reference the same physical properties model, but take into account the presence of melt using scaling relations developed for melting peridotites (e.g., Hammond and Humphreys, 2000). Now

lherzolite \rightarrow harzburgite + dunite with melt + basalt

$$\begin{aligned} \delta\rho/\rho = 0 \rightarrow & (-1\% \text{ to } -2\%, \text{ harzburgite}) \\ & + (-1\% \text{ to } -2\% \text{ dunite w. melt}) \\ & + (-10\%, \text{ basalt}) \end{aligned}$$

$$\begin{aligned} \delta V_p/V_p = 0 \rightarrow & (+0.5\% \text{ to } +1.0\%) + (>-3.6\%) \\ & + (-14\% \text{ to } -16\%) \end{aligned}$$

$$\begin{aligned} \delta V_s/V_s = 0 \rightarrow & (+1\% \text{ to } +1.5\%) + (>-7.9\%) \\ & + (-16\% \text{ to } -23\%). \end{aligned}$$

The relatively large contrasts produced by a small melt fraction in upper mantle peridotites makes their detection by high resolution seismic methods very likely.

3. Imaging considerations

It is well known that tomographic methods relying on infinite frequency approximations to wave propagation

have considerably lower resolution than scattered wave imaging methods. The normal rule of thumb is that tomographic images have resolution that scales with the square root of the product of path length, l , and wavelength, λ , whereas direct imaging methods have resolution proportional to some fraction of a wavelength; half, quarter, and eighth being commonly used coefficients:

$$R_T \propto \sqrt{l\lambda}$$

$$R_S \propto \lambda/b$$

(the original references are Fresnel and Lord Rayleigh, respectively). For smooth continuous interfaces, $\lambda/8$ or better is achievable, whereas for discriminating between two distinct objects, $\lambda/2$ is a more suitable choice. If we use a unit wavelength and a path length of 100 wavelengths, the ratio of R_T/R_S is greater than 10, regardless of the choice of b . In practice neither method achieves resolution as good as the theoretical predictions. Seismic images from both methods are hindered by surface observations providing only one sided coverage of the image area, uneven source distribution in range and azimuth, noise not accounted for in the imaging models, and in the case of scattered wave imaging, imperfections in the velocity model used to focus the image. The latter model is known as the migration velocity model. This underscores the complementary nature of tomographic images that measure velocity variations, and scattered wave imaging, which measure material properties fluctuations. The tomography model is essential to properly focus the scattered wave image. Another serious drawback results from recording profile, rather than areal data, and treating imaging problems as two- or two and a half-dimensional, rather than three-dimensional.

3.1. Fresnel zones and spatial sampling

At present the most serious limitation to scattered wave imaging of the upper mantle is the datasets available. Most portable broadband deployments are made with station spacing so coarse that the images formed are spatially aliased throughout parts of the interesting image space, although recent experiments are attempting to overcome this limitation. Normally station interval is chosen in some tradeoff to maximize both the area of coverage and the resolution of a seismic investigation. In order for an accurate image to be made of a scattering object, at least the first Fresnel zone must be adequately sampled in a Fourier sense. Fresnel radius is a function of target depth, and Fourier sampling

a function of minimum velocity, angle of incidence, and maximum frequency:

$$R_F \approx \sqrt{z_{\text{target}}\lambda}$$

$$\Delta x = \frac{f_{\text{max}} \sin \theta}{2\beta_{\text{min}}}$$

Thus experiment design must balance array length (Fresnel radius), and station density (Fourier sampling), so that

$$N = 2R_f/\Delta x$$

$$N = \frac{4\beta_{\text{min}} \sqrt{z_{\text{target}}\lambda}}{f_{\text{max}} \sin \theta_f}$$

where N is the number of stations needed to adequately sample a target situated directly beneath an array $2R_f$ long, and θ_f is the incidence angle of the signal arriving at the Fresnel radius. In practice array lengths need to be several multiples of the target depth in order to adequately image a target at the maximum depth. Fig. 7 illustrates the dependence of Fresnel radius on frequency, parameterized by target depth using the PREM model to compute wavelengths (Dziewonski and Anderson, 1981). Minimum spatial sampling and array length can be determined from the plot.

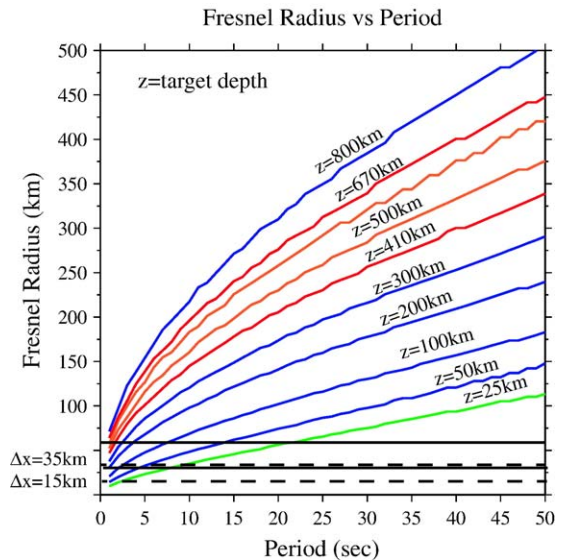


Fig. 7. First Fresnel radius as a function period, parameterized by target depth for P to S scattered waves. To image a point scatterer the first Fresnel zone (twice the Fresnel radius) must be adequately sampled in a Fourier sense. For the arrays described in this study, the spatial sampling intervals and the horizontal Nyquist wavelength are shown as dashed and solid horizontal lines, respectively. See text for a further description of the spatial aliasing criteria.

3.2. Imaging method

The imaging method is based on the Kirchhoff integral, cast to depth migrate individual receiver functions, so that P to S converted waves are repositioned in the subsurface with approximately correct amplitudes. The details of the method are described in Levander et al. (2005b), here we present the imaging equation

$$I(\mathbf{r}) = S_{\text{PS}}(\mathbf{r}) = \frac{c}{4\pi^2} \int_{-\infty}^{\infty} d\omega(i\omega) \int_{-L}^L dS_0 \exp \times \left\{ -i\omega \left(t - [\tau_{\text{P}}(\mathbf{r}_e, \mathbf{r}) + \tau_{\text{S}}(\mathbf{r}, \mathbf{r}_0)] \right) \right\} \times R_{\text{F}}(\mathbf{r}_0, \omega) \frac{A_{\text{S}}(\mathbf{r}, \mathbf{r}_0) \cos\theta(\mathbf{r}_0)}{A_{\text{P}}(\mathbf{r}, \mathbf{r}_e) \beta(\mathbf{r}_0)} \Big|_{t=t_c}$$

where $S_{\text{PS}}(\mathbf{r})$ is the image of the pseudo-PS scattering coefficient (Keho, 1986), ω is frequency, τ_{P} and τ_{S} are the P time from the earthquake to the scattering point, \mathbf{r} , and the S time from the scattering point to the receiver, \mathbf{r}_0 . A_{P} and A_{S} are the P and S amplitudes from the earthquake to the scattering point and from the scattering point to the receiver point, respectively. θ is the incidence angle at the surface, and $\beta(\mathbf{r}_0)$ is surface shear velocity. S_0 is the integration, i.e., recording, surface, which extends $2L$. The complex constant c is determined by the dimensionality of the problem.

The integral can be interpreted as spreading the energy of the receiver function at any time onto a constant traveltimes surface in the subsurface, with appropriate amplitude and obliquity weighting, or as summing all the energy scattered from a single point in the subsurface in the receiver function wavefield along a quasi-hyperboloid (defined by the migration velocity model) back to the scattering point of the subsurface, again with amplitude and obliquity weighting. The migration velocity model is implicit in the traveltimes and amplitude terms.

For a linear array crossing a 2D structure approximately in the dip direction, an additional phase term

$$\Phi(\mathbf{r}, \mathbf{r}_0) = p_y y'$$

can be added to the traveltimes to account for energy arriving out of plane, as described by Bostock et al. (2001). Here p_y is the ray parameter in the local strike

direction, and $y'=0$ is the reference coordinate along which the image is made.

4. Imaging the continental lithosphere

In this section we present three examples of scattered wave images made of the continental lithosphere. The first is from the Kaapvaal Craton, where we are looking for structures at the base of the south African tectosphere. The second two examples are from the North American orogenic plateau, one from the Paleoproterozoic accretionary boundary at the southern edge of the Wyoming Province, the Cheyenne Belt, and the other over a region of recent basaltic magmatism, the Jemez Lineament. In the former we are exploring for accretionary structure, and in the latter remobilization and magmatic structures.

4.1. Kaapvaal craton

Fig. 8 shows pre-stack Kirchhoff depth migrations made from receiver functions from 10 earthquakes recorded at a variety of azimuths by the seismic arrays deployed for the Kaapvaal Seismic Experiment. The depth migration is shown with and without the compressional and shear wave tomography image (James et al., 2001). The stations spacing is on average ~ 35 km along an axis extending from Capetown, South Africa, to the Zimbabwe craton (~ 2000 km), making the array useful for imaging deep structures (>250 km, see Fig. 7), but poor for wavefield imaging of the shallower lithosphere. Crustal reverberations extend to $\sim 200+$ km depth south of the Kaapvaal craton, where the crust is ~ 40 km thick, and to ~ 150 – 200 km beneath the craton, where the crust is ~ 35 km thick (Nguuri et al., 2001; Niu and James, 2002). The receiver function data were bandpass filtered from 0.033 to 0.167 Hz (Fig. 8A) and 0.033 to 0.33 Hz (Fig. 8B). The final images were made with subimages dip-restricted to retain S waves within 45° of the incident P-wave.

The array crosses a series of Proterozoic mobile belts, the Kaapvaal craton and the Bushveld complex, the Proterozoic Limpopo belt, and ends in the Zimbabwe craton. Tomographic images place the base of the craton at 250–300 km under the Kaapvaal craton, with reduced velocity under the Bushveld complex. The tomography puts the base of the Zimbabwe craton at depths of ~ 200 km.

The image in Fig. 8A shows the 410 and 660 discontinuities very clearly, with the 410 clearest under the Kaapvaal craton, and the 660 across almost the entire image. The 410 is at an average depth of $411.5 \pm$

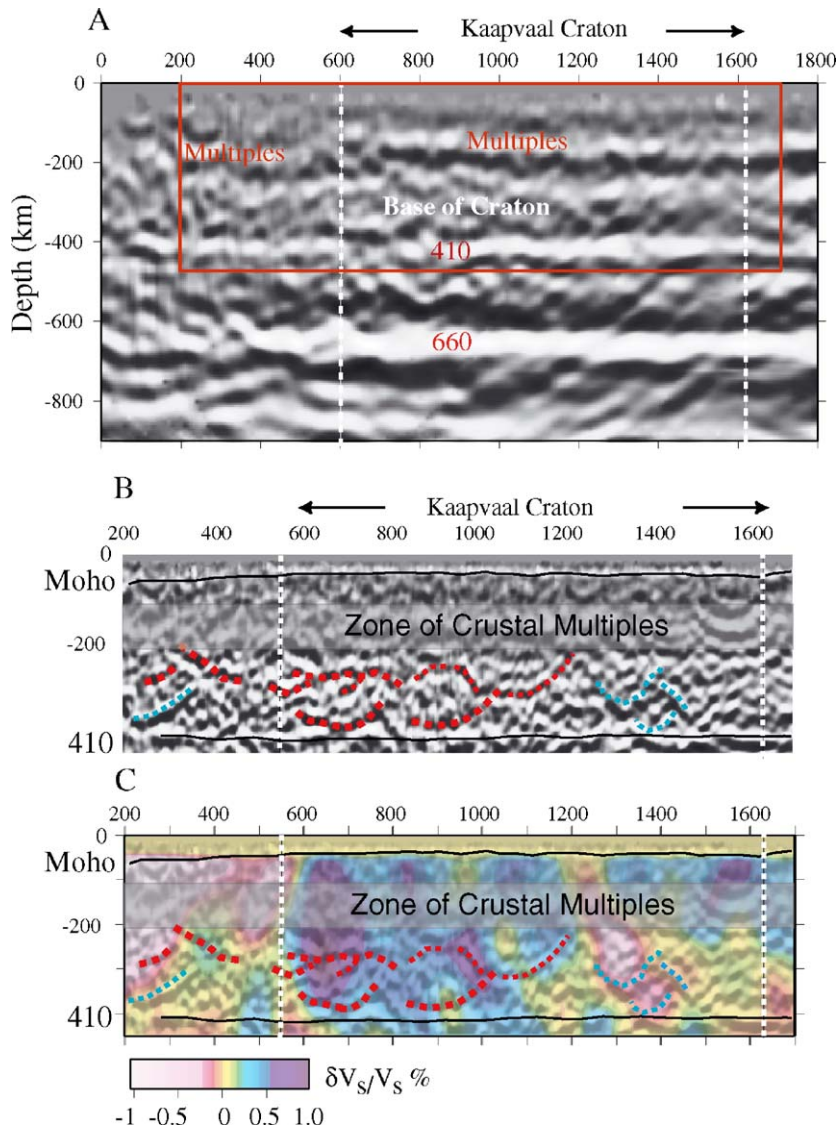


Fig. 8. A) Pre-stack Kirchoff depth migration of receiver functions from 10 earthquakes recorded by the Kaapvaal seismic array (see Levander et al., 2005b, or James et al., 2001 for a location map). The data were bandpass filtered from 0.033–0.167 Hz, and the final image was dip-filtered to include scattering angles to 45° from the P waves. B) Pre-stack depth migrated image with of upper 425 km using a bandpass of 0.033–0.33 Hz to examine detail at the base of the craton between the crustal multiples and the 410 discontinuity. C) Same image as B with S-wave tomography fluctuation used in depth migration superimposed. The tomography model is from James et al. (2001). The background 1-D model is a modified IASP91 model (Niu et al., 2004; Kennett and Engdahl, 1991). The transition zone discontinuities in A are extremely well imaged, particularly directly beneath the craton. Between the zone of crustal multiples and the top of the transition zone are a series of continuous positive and negative events extending 100s of kilometers that we interpret as conversions from structures associated with the base of the tectosphere. See text for details.

10.6 km from $X=0$ to $X=1800$ km. This is approximately the same depth as previous estimates by these authors (Niu et al., 2004), and 15 km deeper than estimates by Gao et al. (2002). The 660 is at an average depth of 648.5 ± 14.6 km. The variance is large because of a poorly formed image from $X=100$ to $X=600$ km, as well as the natural wavelength increase

with depth. This corresponds reasonably well to previous estimates, and gives a transition zone thickness of 237.0 ± 18.0 km, about 5–6 km less than global averages.

The average amplitude ratio of the 660 to 410 in the image is 2.06, which compares well with the ratios of the PREM predictions for shear and shear impedance of

about 1.83, and 1.86, respectively (synthetic tests demonstrate that we can recover amplitude ratios with about 10% error). We have also calculated that the pulse spread of the signal from the 660 compared to the 410 is about a factor of 1.57 using a common definition of signal width (Papoulis, 1975). The expected spread from the increase of velocity with depth predicted by PREM is 1.2. This corresponds to a 660 discontinuity width that is on average 1.31 times larger than the width of the 410 discontinuity. Beneath the Kaapvaal craton, where the 660 discontinuity width is noticeably larger, the pulse width ratio is 1.87, giving a ratio for the 660 to 410 discontinuity widths of 1.56.

The base of the craton is not a prominent horizon like the 410 and 660. Synthetic tests (Levander et al., 2005b) indicate that the Kaapvaal array should be able to image a continuous interface with a -1.5% velocity decrease with depth as shallow as 250–275 km before the signals are overwhelmed by crustal multiple energy. Fig. 8B–C show the higher frequency (0.033–0.33 Hz) migration of the data to just below the 410 discontinuity. Between the multiple train and the top of the transition zone are a series of relatively weak negative events that follow the base of the high velocities interpreted as the base of the tectosphere (James et al., 2001). Note that these events are continuous over distances of several hundred kilometers, are of the same lateral extent as the positive and negative tomography anomalies, and appear short only in comparison to the 410 and 660 in Fig. 8A. These events are on average about 80% of the size of the 410 event in amplitude, suggesting shear impedance contrasts of about -2% to -3% , in relatively good agreement with the predictions for the contrast between more fertile and less fertile mantle as well as that between eclogite and more fertile mantle. Subduction and accretion of Precambrian oceanic plates to form or stabilize a cratonic root would produce structures with alternating positive and negative velocity contrasts with a lateral extent of hundreds of kilometers (e.g., Snyder, 2002; Cooper et al., 2006). The top of the oceanic lithosphere would contain converting surfaces at interfaces between eclogitized oceanic crust (garnet pyroxenites) over depleted harzburgites, and at the depleted harzburgite over a less depleted lherzolite. Stacking lithospheric columns would repeat the sequence of negative and positive converting surfaces.

4.2. *Cheyenne belt*

A major target of the CD-ROM seismic investigations was the Cheyenne Belt, which in outcrop

juxtaposes Paleoproterozoic island arc rocks against an Archean passive margin sequence across a narrow south dipping boundary. This terrane suture formed during Paleoproterozoic collision of island arc terranes with a passive margin on the southern edge of the Archean Wyoming province. One of the DeepProbe and CD-ROM goals was to determine whether or not the Cheyenne belt persists into the upper mantle using reflection, refraction, and teleseismic data. Deep Probe seismic refraction data indicate that the upper mantle changes from tectonic to cratonic over a distance of no more than 250 to 300 km across this boundary (Henstock and the Deep Probe Working Group, 1998). The reflection data from CD-ROM were interpreted as showing a north dipping suture zone that extends to Moho depths (Morozova et al., 2005). The CD-ROM refraction data identify a high velocity uplift to the north of the surface trace of the Cheyenne belt, but failed to identify any substantial upper mantle variations, largely due to aperture limitations (Levander et al., 2005a). One CD-ROM passive array composed of 15 instruments spaced at ~ 15 km intervals crossed the Cheyenne Belt (Fig. 9). From this array we can image the lithosphere above the zone of multiples starting at ~ 175 km with frequencies as high as 0.333 Hz (refer to Fig. 7). CD-ROM teleseismic tomography (Yuan and Dueker, 2005) images a north dipping, high velocity ($+2.6\% V_p$, $+7.8\% V_s$) body extending from the base of the crust to depths greater than 200 km which they interpret as a remnant of a subducting slab left from Paleoproterozoic (~ 1.70 – 1.75 Ga) accretion of island arc terranes to the southern edge of the Wyoming province proto-continent.

The migration velocity models for this and the Jemez Lineament model described below were constructed from Yuan and Dueker's one-dimensional reference model with the 2-D fluctuations from the tomography added. The crustal model for the migration was taken directly by subsampling the CD-ROM refraction model (Levander et al., 2005a). Receiver functions made from the CD-ROM data for both the Cheyenne Belt, and the Jemez Lineament were provided by Zurek and Dueker (2005). Fig. 10 shows the prestack depth migrated image made from 7 earthquakes recorded across the CD-ROM Cheyenne Belt array, together with the refraction data, a reflection interpretation, and the P tomography image.

The migrated image of the Cheyenne Belt (Fig. 10) shows the Moho at ~ 50 km depth, in good agreement with the refraction Moho. Just below the Moho, beginning at lateral coordinate 150 km and extending to approximately coordinate 25 km (Fig. 10) are a pair of

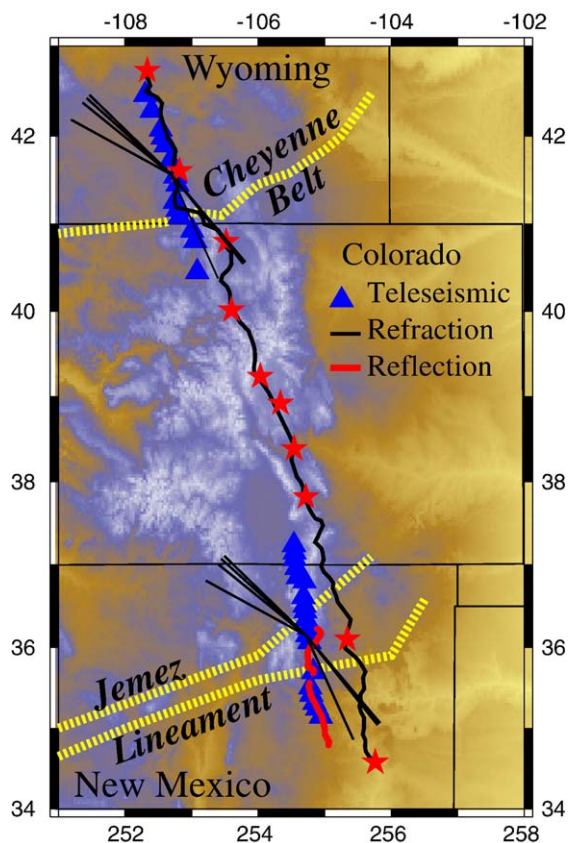


Fig. 9. Location map of the CD-ROM seismic experiments, showing the location of two of the principal Paleoproterozoic boundaries, the Cheyenne Belt and the Yavapia–Mazatzal boundary which is coincident with the Quaternary–Neogene Jemez Lineament. The CD-ROM teleseismic arrays (triangles) and reflection profiles (thick solid lines) were centered over the two boundaries, the CD-ROM refraction experiment (thin solid line and stars) extended continuously from north-central New Mexico to southern Wyoming. Earthquake back-azimuths are shown as straight lines centered on each of the teleseismic arrays.

north-dipping positive and negative polarity events. The high velocity P and S anomaly lies largely between these two events. A converted S wave from the bottom of the high velocity body would be negative polarity, indicative of a change from low to high impedance. Similarly a shear conversion from the top of the high velocity body would show a positive polarity. We therefore interpret these two events as bounding the high velocity body.

In the depth migrated receiver function image, the Moho immediately above the high velocity north dipping body is broken in the same region that wide-angle active source data failed to detect a PmP reflection, and where the interpretation of the CD-ROM reflection data indicates the subsurface suture between the Archean and Proterozoic terranes.

The image is likely complicated by three factors, one related to the regional structure and the other two to the local structure. In map view the Cheyenne belt makes a broad arc to the northeast beginning roughly at the crossing of the CD-ROM teleseismic line. This makes the 2.5-D assumption for migrating the data somewhat inaccurate. The local structural features that complicate the image are the presence of a deep sedimentary basin on the north edge of the array, which contributes scattered surface waves to the receiver functions, and the mismatch in high P and S velocities in the tomography models. As the receiver functions are sensitive to S-wave perturbations and density perturbations, and the density perturbations for depleted peridotite are large and negatively correlated with both P and S perturbations (Fig. 5), the image is a combination of scattered waves resulting from both types of perturbation, which in this case may not be coincident.

4.3. Jemez lineament

The Jemez Lineament is defined by a trend of Neogene volcanics extending from the eastern Colorado–New Mexico border to south-central Arizona, and coincides with a Paleoproterozoic suture zone separating island arc terranes accreted to North America at about 1.70–1.75 Ga (Fig. 9). The Jemez lineament was the other major target of the CD-ROM active and passive seismic experiments (Karlstrom and CD-ROM Working Group, 2002). Jemez lineament basalt flows as young as 800 ka are found outcropping along the CD-ROM seismic corridor within the teleseismic array and reflection survey. Seismic reflection profiling has identified a Paleoproterozoic bivergent orogen, nappes of which outcrop in the Sangre de Cristo. A series of bright reflections as depths of 10 to 15 km are interpreted as mafic sills related to Jemez Lineament mafic volcanism (Magnani et al., 2004, 2005).

One CD-ROM passive array composed of 15 instruments spaced at ~15 km intervals crossed the Jemez lineament (Fig. 9). From this array we can image the lithosphere above the zone of multiples with frequencies as high as 0.333 Hz (refer to Fig. 7). Fig. 11 shows a migrated receiver function image with reflection and refraction interpretations superimposed. The crust is ~40 km thick, and is reflective almost to its base, except in the region immediately north of the southern edge of the Jemez Lineament. The refraction data show that the crust is thinned slightly beneath the outcrop of recent volcanic activity ($X=75$ – 175 km in Fig. 9; Levander et al., 2005b), in the same region that lower crustal reflectivity is weak or absent (Magnani et

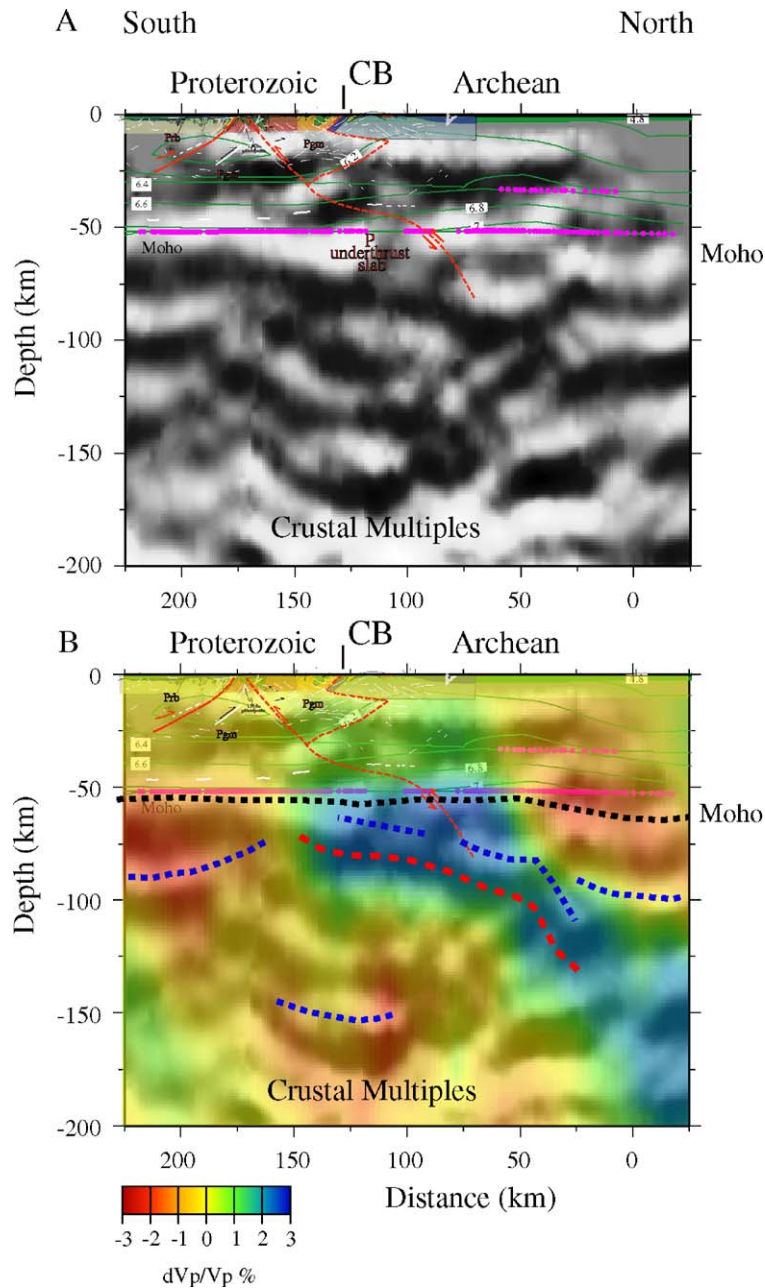


Fig. 10. Cheyenne Belt pre-stack Kirchhoff depth migrated receiver function image made from data from 7 earthquakes (top) shown with the P-wave tomography fluctuations used in the migration (bottom). The receiver function data were bandpass filtered from 0.033–0.33 Hz, and the final image was made with subimages preserving scattered S-waves within 45° of the incident P-waves. The Moho is well imaged and corresponds well to the Moho determined from the refraction data. The mismatches in depth to the Moho from the refraction and receiver function images results from the complex Moho structure (see Keller et al., 2005) being illuminated from above and from below. The image is complicated but shows a positive polarity north dipping event (dashed blue line) above a negative polarity north dipping event (dashed red line) that outlines the positive P (and S) wave anomaly in the north central part of the section, interpreted as a remnant subducting slab by Yuan and Dueker (2005). Positive polarity events (dashed blue lines) correspond to a negative velocity anomaly directly below the Moho at the southern end of the section. See text for details. Tomography image fluctuations are from Yuan and Dueker, 2005. The background 1-D model is a modified IASP91 model (Kennett and Engdahl, 1991).

al., 2005). Surface heat flow in this region is high to very high ($>100 \text{ mW/m}^2$). The refraction data show low Pn velocities ($\sim 7.75 \text{ km/s}$) from which we estimated that the upper mantle contains $\sim 1\%$ partial melt using the relations of Hammond and Humphreys (2000). Beneath this region, P and S wave tomography show -3% and -5% anomalies, located for the most part

above $\sim 150 \text{ km}$ depth (Fig. 11B; Yuan and Dueker, 2005).

We used the refraction derived velocity model of the crust (Levander et al., 2005b), and the 2-D tomography anomalies of Yuan and Dueker (2005) added to their 1D reference model of the mantle to construct the migration velocity model. The depth migrated receiver functions

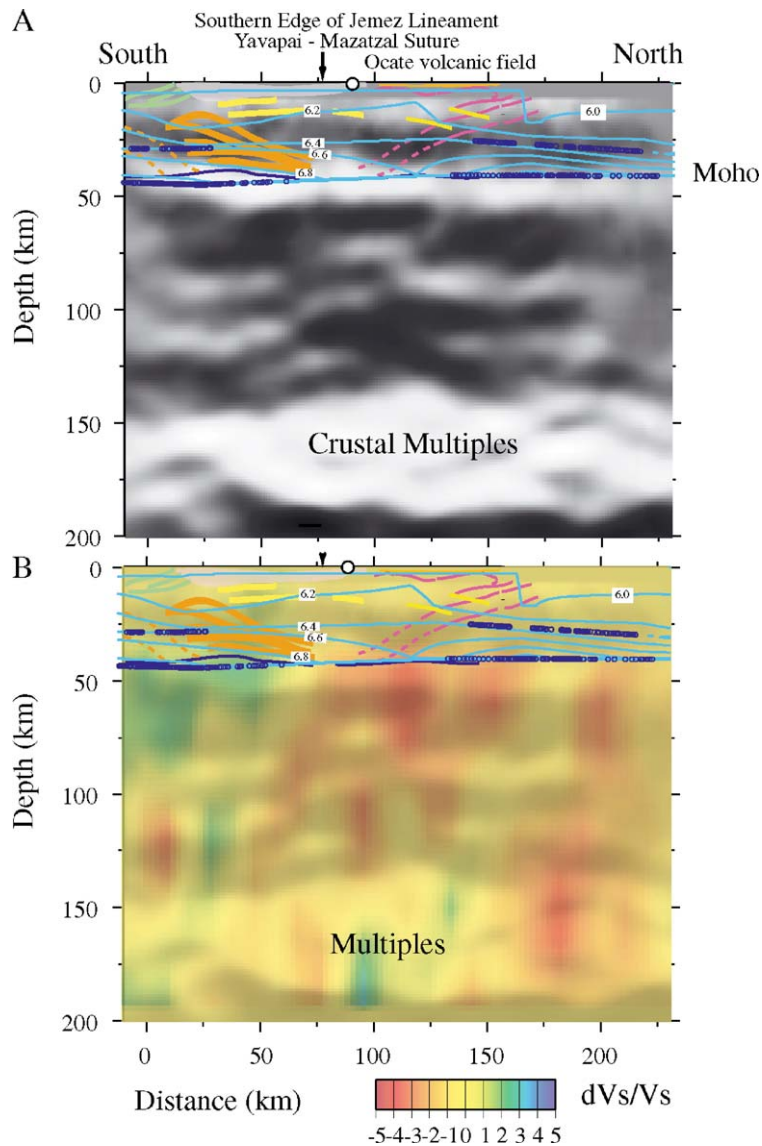


Fig. 11. A) Jemez Lineament pre-stack Kirchhoff depth migrated receiver function image made from data from 7 earthquakes shown with refraction velocity contours (blue) and reflection interpretation from crustal data. The receiver function data were bandpass filtered from 0.033–0.33 Hz, and the final image was made with subimages preserving scattered S-waves within 45° of the incident P-waves. The Moho is well imaged and corresponds well to the Moho determined from the refraction data. The mismatches in depth to the Moho from the refraction and receiver function images results from the complex Moho structure (see Keller et al., 2005) being illuminated from above and from below. B) Same image with S wave tomography fluctuations used in migration model superimposed. Tomography from Yuan and Dueker (2005). The background 1-D model is a modified IASP91 model (Kennett and Engdahl, 1991). C) The same image with large amplitude negative polarity sill like structures shown in solid red. We interpret these as melt producing zones.

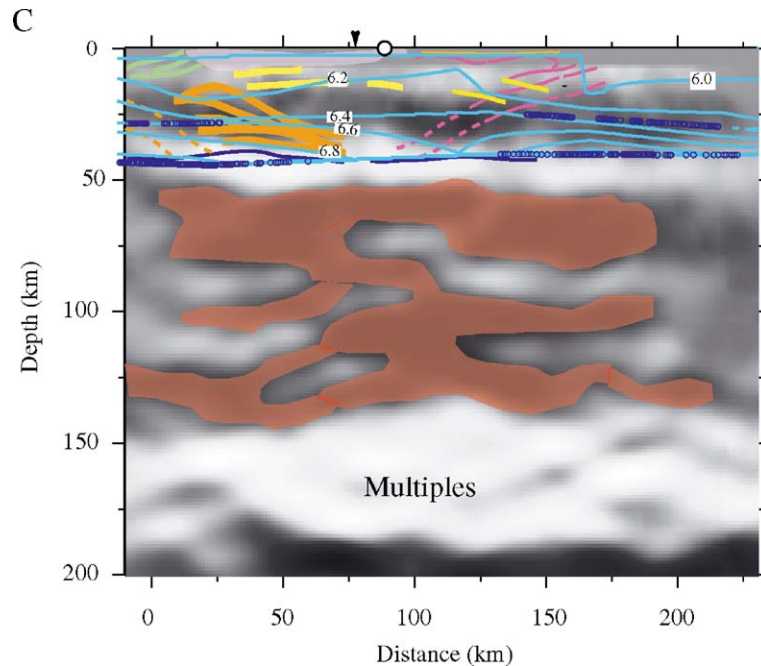


Fig. 11 (continued).

image the Moho well, placing it at the same level as the refraction data, beneath which are a complex layered pattern between the Moho and the zone of crustal multiple reflections starting at ~ 150 km depth. The layers are 15–20 km in thickness, and extend laterally ~ 100 km. The amplitudes of the negative anomalies in the layered zone are comparable in strength to the Moho signals. The positive amplitudes in the anomaly zone are considerably weaker ($>25\%$) than the size of the negative amplitudes.

We interpret these as layers of melt production in fertile mantle alternating with higher velocity less fertile mantle (Fig. 11C). The patterns look like a system of sills extending to at least 125 km depth. The tomography shows this as a continuous body extending to similar depths, with a 5% reduction in shear velocity, comparable in size to the shear velocity contrast at the Moho in the migration velocity model. The pre-stack depth migrated images show that the Moho conversion and the mantle conversions are similar in size, but of opposite sign, therefore we infer that the sills have velocity contrasts with the surrounding mantle at least as large as that at the Moho. Although we don't have a direct measurement of S velocity contrast at the Moho we infer that it is at least as large as -10% , estimated from the compressional wave refraction data and converting to S wave velocities. Given that roughly half of the mantle is occupied by the sill structures beneath the Jemez Lineament, an estimate of -10% is

in keeping with a -5% average for the entire upper 100 km of the mantle. Where the heat source for the melt originates is unclear, either the melt drains upward from a partially molten, deeper asthenospheric source, or asthenospheric mantle has invaded the ancient suture between the Yavapai and Mazatzal island arc terranes, producing melt as it decompresses (see Magnani et al., 2005).

5. Discussion

We feel that the most compelling feature of the three images that we have presented are the sill-like structures that produce bright conversions that reside in the mantle beneath the Jemez Lineament magmatic system (Fig. 11). The transition zone discontinuities beneath the Kaapvaal craton (Fig. 8) are very clearly seen in the prestack depth migrations, but have been observed before with simple common conversion point stacks (e.g., Niu et al., 2004). The base of the Kaapvaal craton is very complicated and is difficult to interpret in a simple fashion. The inferred paleo-slab beneath the Cheyenne Belt is imaged as a complicated structure in both the receiver functions and the regional tomography (see Zurek and Dueker, 2005; Fig. 10).

The internal structure of magmatic systems associated with basalt extraction has been inferred from the structure of ophiolites, but not observed

teleseismically with any detail beyond the overall structure of the melt producing zone, as in the results from the MELT experiment. In the active source bandwidth the details of the structures of the axial magma chamber at the EPR have been determined using 2 and 3 dimensional reflection profiling (Mutter et al., 1995; Hussenoeder et al., 1996), but signal penetration beneath the axial magma chamber is generally imperfect. On land we have observed a similar pattern of brightly reflecting sills within the lower crust south of the Mendocino Triple Junction (Levander et al., 1998; Henstock and Levander, 2000), in a tectonic environment from which basaltic magmas erupt periodically. The image we present here of a likely melt producing zone beneath the Jemez lineament provides an intermediate scale between body or surface wave tomography, and active source reflection/refraction profiling. The features are ~10 km in thickness, and 50–100 km laterally.

6. Conclusions

We have reviewed aspects of what is known about upper mantle structures beneath the continents that we feel is relevant to the scales intermediate between the large scales imaged in global and regional tomography, and the small scales observed in reflection profiles or in outcrops of ophiolites and peridotite massifs. We have included some information on what types of seismic velocity and density contrasts can be expected between the different tectonic elements at these intermediate scales that result from the two primary processes now affecting the upper mantle, and likely to have affected it since continents began to form: Subduction and melt extraction.

We present a means of imaging shear velocity and density structures in this intermediate scale range, using the Kirchhoff integral to depth migrate receiver functions. A limiting constraint on imaging with teleseismic array recordings is that the arrays have adequate station density to avoid spatial aliasing problems. The images of the Jemez Lineament upper mantle and the Kaapvaal craton transition zone are quite clear and match the expectations we have for each of the structures: In the former case, we have imaged sill-like melt-producing structures extending to depths of 125 km. In the latter case, we image bright conversions from a nearly flat discontinuity structure under the Kaapvaal craton. The amplitudes of the conversions, and the discontinuity widths are consistent with global observations of transition zone discontinuity structure.

Acknowledgements

The authors thank K. Dueker, B. Zurek, and H. Yuan for tomography models and receiver functions from the CD-ROM passive experiments, and D. James for the tomography models and receiver function data from the Kaapvaal Seismic Experiment. This research was supported by grants from the NSF Continental Dynamics and NSF Collaborative Math-Geoscience Programs.

References

- Aki, K., Richards, P.G., 1980. *Quantitative Seismology; Theory and Methods*. W.H. Freeman and Co., San Francisco, Calif., United States.
- Allegre, C.J., Turcotte, D.L., 1986. Implications of a two-component marble-cake mantle. *Nature* 323, 123–127.
- Bostock, M.G., 1998. Mantle stratigraphy and evolution of the Slave province. *J. Geophys. Res.* 103, 21193–21200.
- Bostock, M.G., Rondenay, S., Schragge, D.S., 2001. Multiparameter two-dimensional version of scattered teleseismic body waves: 1. Theory for oblique incidence. *J. Geophys. Res.* 106, 30771–30782.
- Braun, M.G., Keleman, P.B., 2002. Dunite distribution in the Oman ophiolite: implications for melt flux through porous dunite conduits. *Geochem. Geophys.* 3. doi:10.1029/2001GC000289.
- Calvert, A.J., Sawyer, E.W., Davis, W.J., Ludden, J.N., 1995. Archean subduction inferred from seismic images of a mantle suture in the Superior Province. *Nature* 375, 670–674.
- Christensen, N.I., 1978. Ophiolites, seismic velocities and oceanic crustal structure. *Tectonophysics* 47, 131–157.
- Christensen, N.I., Mooney, W.D., 1995. Seismic velocity structure and composition of the continental crust: a global view. *J. Geophys. Res.* 100, 9761–9788.
- Christensen, N.I., Salisbury, 1975. Structure and constitution of the lower oceanic crust. *Rev. Geophys. Space Phys.* 13, 57–86.
- Cleary, J.R., Haddon, R.A., 1972. Seismic wave scattering near the core–mantle boundary: a new interpretation of precursors to PKP. *Nature* 240, 549–551.
- Cook, F.A., van der Velden, A.J., Hall, K.W., Roberts, B.J., 1998. Frozen subduction in Canada's Northwest Territories: lithoprobe deep lithospheric reflection profiling of the western Canadian shield. *Tectonics* 18, 1–24.
- Cooper, C.M., Lenardic, A., Levander, A., Moresi, L., 2006. Creation and preservation of cratonic lithosphere: seismic constraints and geodynamic models. In: Benn, K., Mareschal, J.-C., Condie, K.C. (Eds.), *Archean Geodynamics and Environments*, Geophysical Monograph, 164. American Geophysical Union, Washington, D.C., pp. 75–88. doi:10.1029/164GM07.
- Dziewonski, A.M., Anderson, D.L., 1981. Preliminary reference Earth Model (PREM). *Phys. Earth Planet. Inter.* 25, 297–356.
- Gao, S.S., Silver, P.G., Liu, K.H., Kaapvaal Seismic Group, 2002. Mantle discontinuities beneath Southern Africa. *Geophys. Res. Lett.* 29. doi:10.1029/2001GL013834.
- Grand, S., 1994. Mantle shear structure beneath the Americas and surrounding oceans. *J. Geophys. Res.* 99, 11591–11621.
- Gulick, S.P.S., Meltzer, A.S., Henstock, T.J., Levander, A., 2001. Internal deformation of the southern Gorda plate: fragmentation of a weak plate at the Mendocino triple junction. *Geology* 29, 691–694.

- Hammond, W.C., Humphreys, E.D., 2000. Upper mantle seismic wave velocities: effects of realistic partial melt geometries. *J. Geophys. Res.* 105, 10975–10986.
- Hedlin, M.A.H., Shearer, P.M., 2000. An analysis of large-scale variations in small-scale mantle heterogeneity using Global Seismographic Network recordings of precursors to PKP. *J. Geophys. Res.* 105, 13655–13673.
- Henstock, T.J., the Deep Probe Working Group, 1998. Probing the Archean and Proterozoic lithosphere of western North America. *GSA Today*, 8: 1–5 & 16–17.
- Henstock, T.J., Levander, A., 2000. Impact of a complex overburden on analysis of bright reflections: a case study from the Mendocino Triple Junction. *J. Geophys. Res.* 105, 21711–21726.
- Humphreys, E.D., Duker, K.G., 1994a. P-velocity structure of the western U.S. *J. Geophys. Res.* 99, 9615–9634.
- Humphreys, E.D., Duker, K.G., 1994b. Physical state of the western U.S. upper mantle. *J. Geophys. Res.* 99, 9635–9650.
- Hunt, D.L., Kellogg, L.H., 2001. Quantifying mixing and age variations of heterogeneities in models of mantle convection: role of depth dependent viscosity. *J. Geophys. Res.* 106, 6747–6759.
- Hussenoeder, S.A., Collins, J.A., Kent, G.M., Detrick, R.S., 1996. Seismic analysis of the axial magma chamber reflector along the southern East Pacific Rise from conventional reflection profiling. *J. Geophys. Res.* 101 (10), 22087–22105.
- James, D.E., Fouch, M.J., et al., 2001. Tectospheric structure beneath Southern Africa. *Geophys. Res. Lett.* 28, 2485–2488.
- Jordan, T.H., 1978. Composition and development of the continental tectosphere. *Nature* 274, 544–548.
- Jordan, T.H., 1988. Structure and formation of the continental tectosphere. *J. Petrol.* 11–37 (Special Lithosphere Issue).
- Kaneshima, Helffrich, 1998. Detection of lower mantle scatterers northeast of the Marianna subduction zone using short-period array data. *J. Geophys. Res.* 103, 4825–4838.
- Kaneshima, S., Helffrich, G., 1999. Dipping lower-velocity layer in the mid-lower mantle: evidence for geochemical heterogeneity. *Science* 283, 1888–1891.
- Karlstrom, K., CD-ROM Working Group, 2002. Structure and evolution of the lithosphere beneath the Rocky Mountains. *GSA Today* 4–10.
- Keho, T.H., 1986. The vertical seismic profile: imaging in heterogeneous media. *Earth, Atmospheric, and Planetary Sciences*. MIT, Cambridge, MA, p. 304.
- Keller, G.R., Karlstrom, K.E., Williams, M.L., Miller, K.C., Andronicos, C., Levander, A., Snelson, C., Prodehl, C., 2005. The dynamic nature of the continental crust–mantle boundary: crustal evolution in the southern Rocky Mountain region as an example. In: Karlstrom, K., Keller, G.R. (Eds.), *The Rocky Mountains: An Evolving Lithosphere*, Geophysical Monograph Series, 154. American Geophysical Union, Washington, D.C., pp. 403–420. doi:10.1029/154GM30.
- Kellogg, L.H., Turcotte, D.L., 1990. Mixing and the distribution of heterogeneities in a chaotically convecting mantle. *J. Geophys. Res.* 95, 421–432.
- Kellogg, J.B., Jacobsen, S.B., O'Connell, R.J., 2002. Modeling the distribution of isotopic ratios in geochemical reservoirs. *EPSL* 204, 183–202.
- Kennett, B.L.N., Engdahl, E.R., 1991. Traveltimes for global earthquake location and phase identification. *Geophys. J. Int.* 105, 429–465.
- Lee, C.-T.A., 2003. Compositional variation of density and seismic velocities in natural peridotites at STP conditions: implications for seismic imaging of compositional heterogeneities in the upper mantle. *J. Geophys. Res.* 108. doi:10.1029/2003JB002413.
- Levander, A., Nolet, G., 2005. *Seismic Earth: Array Analysis of Broadband Seismograms*, Geophysical Monograph Series, 157. American Geophysical Union, Washington, D.C. 280 pp. doi:10.1029/157GM00.
- Levander, A., Henstock, T.J., Meltzer, A.S., Beaudoin, B.C., Trehu, A.M., Klemperer, S.L., 1998. Fluids in the lower crust following Mendocino Triple Junction migration: active basaltic intrusion? *Geology* 26, 171–174.
- Levander, A., Zelt, C.A., Magnani, M.B., 2005a. Crust and upper mantle velocity structure of the southern Rocky Mountains from the Jemez Lineament to the Cheyenne Belt. In: Karlstrom, K., Keller, G.R. (Eds.), *The Rocky Mountains: An Evolving Lithosphere*, Geophysical Monograph Series, 154. American Geophysical Union, Washington, D.C., pp. 293–308. doi:10.1029/154GM22.
- Levander, A., Niu, F., Symes, W.W., 2005b. Imaging teleseismic P to S scattered waves using the Kirchhoff integral. In: Levander, A., Nolet, G. (Eds.), *Seismic Earth: Array Analysis of Broadband Seismograms*, Geophysical Monograph Series, 157. American Geophysical Union, Washington, D.C., pp. 149–169. doi:10.1029/156GM10.
- Magnani, M.B., Miller, K.M., Levander, A., Karlstrom, K., 2004. The Yavapai–Mazatzal boundary: a long-lived tectonic element in the lithosphere of southwestern North America. *Geol. Soc. Amer. Bull.* 116, 1137–1142.
- Magnani, M.B., Levander, A., Miller, K.M., Eshete, T., Karlstrom, K.E., 2005. Seismic investigation of the Yavapai–Mazatzal transition zone and the Jemez Lineament in northeastern New Mexico. In: Karlstrom, K., Keller, G.R. (Eds.), *The Rocky Mountains: An Evolving Lithosphere*, Geophysical Monograph Series, 154. American Geophysical Union, Washington, D.C., pp. 227–238. doi:10.1029/154GM16.
- Meibom, A., Anderson, D.L., 2003. The statistical upper mantle assemblage. *Earth Planet. Sci. Lett.* 217, 123–139.
- MELT Seismic Team, 1998. Imaging the deep seismic structure beneath a mid-ocean ridge: the MELT experiment. *Science* 280, 1215–1218.
- Morozova, E., Wan, X., Chamberlain, K., Smithson, S., Johnson, R., Karlstrom, K., 2005. Inter-wedging nature of the Cheyenne Belt–Archean–Proterozoic suture from seismic reflection data. In: Karlstrom, K.E., Keller, G.R. (Eds.), *Lithospheric Structure and Evolution of the Rocky Mountain Region*. American Geophysical Union, Washington, D.C.
- Mutter, J.C., Carbotte, S.M., Su, W., Xu, L., Buhl, P., Detrick, R.S., Orcutt, J.A., Harding, A.J., 1995. Seismic images of active magma systems beneath the East Pacific Rise between 17 degrees 05' and 17 degrees 35'S. *Science* 268, 391–395.
- Nguiri, T.K., Gore, J., James, D.E., Webb, S.J., Wright, C., Zengeni, T.G., Gwavana, O., Snoke, J.A., Kaapvaal Seismic Group, 2001. Crustal structure beneath southern Africa and its implications for the formation and evolution of the Kaapvaal and Zimbabwe Cratons. *Geophys. Res. Lett.* 28, 2501–2504.
- Niu, F., James, D.E., 2002. Fine structure of the lowermost crust beneath the Kaapvaal Craton and its implications for crustal formation and evolution. *Earth Planet. Sci. Lett.* 200, 121–130.
- Niu, F., Kawakatsu, H., Fukao, Y., 2003. Seismic evidence for a chemical heterogeneity in the mid-mantle: a strong and slightly dipping seismic reflector beneath the Mariana subduction zone. *J. Geophys. Res.* 108. doi:10.1029/2002JB002384.

- Niu, F., Levander, A., Cooper, C.M., Lee, C.-T.A., Lenardic, A., James, D.E., 2004. Seismic constraints on the depth and composition of the mantle keel beneath the Kaapvaal Craton. *Earth Planet. Sci. Lett.* 224, 337–346.
- Papoulis, N., 1975. *Signal Analysis*. Harcourt Brace, New York.
- Polet, J., Anderson, D.L., 1995. Depth extent of cratons as inferred from tomographic studies. *Geology* 23, 205–208.
- Pollack, H.N., 1986. Cratonization and thermal evolution of the mantle. *Earth Planet. Sci. Lett.* 80, 175–182.
- Snyder, D.B., 2002. Lithospheric growth at margins of cratons. *Tectonophysics* 355, 7–22.
- Van der Lee, S., Nolet, G., 1997. Upper mantle S velocity structure of North America. *J. Geophys. Res.* 102, 22815–22838.
- Webb, S.C., Forsythe, D.W., 1998. Structure of the upper mantle under the EPR from waveform inversion of regional events. *Science* 280, 1227–1229.
- Wu, R.-S., Aki, K., 1985. Scattering characteristics of elastic waves by an elastic heterogeneity. *Geophysics* 50, 582–595.
- Yuan, H., Dueker, K., 2005. Upper mantle tomographic V_p and V_s images of the middle Rocky Mountains in Wyoming, Colorado, and New Mexico: evidence for a thick heterogeneous chemical lithosphere. In: Karlstrom, K., Keller, G.R. (Eds.), *The Rocky Mountains: An Evolving Lithosphere*, Geophysical Monograph Series, 154. American Geophysical Union, Washington, D.C., pp. 329–346. doi:10.1029/154GM25.
- Zurek, B., Dueker, K., 2005. Lithospheric stratigraphy beneath the southern Rocky Mountains. In: Karlstrom, K., Keller, G.R. (Eds.), *The Rocky Mountains: An Evolving Lithosphere*, Geophysical Monograph Series, 154. American Geophysical Union, Washington, D.C., pp. 317–328. doi:10.1029/154GM24.